Imaging crystal stress in diamond using ensembles of nitrogen-vacancy centers

P. Kehayias,[1,2,*] M. J. Turner,[1,3] R. Trubko,[1,4] J. M. Schloss,[3,5] C. A. Hart,[1]
M. Wesson,[6] D. R. Glenn,[1] and R. L. Walsworth[1,2,3]

[1]*Department of Physics, Harvard University, Cambridge, Massachusetts 02138, USA*
[2]*Harvard-Smithsonian Center for Astrophysics, Cambridge, Massachusetts 02138, USA*
[3]*Center for Brain Science, Harvard University, Cambridge, Massachusetts 02138, USA*
[4]*Department of Earth and Planetary Sciences, Harvard University, Cambridge, Massachusetts 02138, USA*
[5]*Department of Physics, Massachusetts Institute of Technology, Cambridge, Massachusetts 02139, USA*
[6]*Department of Physics, University of Chicago, Chicago, Illinois 60637, USA*

(Received 26 August 2019; published 11 November 2019)

We present a micrometer-scale-resolution stress imaging method with millimeter field-of-view for diamonds containing a thin surface layer of nitrogen-vacancy (NV) centers. In this method, we reconstruct stress tensor elements over a two-dimensional field of view from NV optically detected magnetic resonance (ODMR) spectra. We use this technique to study how stress inhomogeneity affects NV magnetometry performance and show how NV $M_{z,\kappa}$ imaging is a useful and direct way to assess these effects. This tool for mapping stress in diamond will aid optimization of NV-diamond sensing, with wide-ranging applications in the physical and life sciences.

DOI: 10.1103/PhysRevB.100.174103

Nitrogen-vacancy (NV) color centers in diamond are an increasingly popular tool for sensing and imaging electromagnetic fields and temperature, with wide-ranging applications. In particular, wide-field two-dimensional (2D) magnetic imaging using ensembles of NV centers can provide micrometer spatial resolution and millimeter field of view in ambient conditions, enabling investigations of condensed-matter physics, paleomagnetism, and biomagnetism problems [1–5]. However, one limitation to an NV magnetic imager's sensitivity is intrinsic diamond stress variation, which inhomogeneously shifts the NV ground-state resonance frequencies and spoils the NV spin dephasing time [6]. Diamond crystal stress and strain are therefore important to understand and minimize when optimizing NV magnetometry [7,8] and magnetic microscopy.

In this work, we use an ensemble NV surface layer to image diamond stress across a millimeter-scale field of view and explore how stress inhomogeneity impedes NV magnetic microscopy. A 532-nm laser illuminates the micrometer-scale NV layer at the top surface of a diamond chip (4 mm × 4 mm wide and 0.5 mm thick) and an optical microscope images the spin-state-dependent NV fluorescence onto a camera (Fig. 1). Probing the transition frequencies between NV ground-state sublevels by sweeping the frequency of an applied microwave field yields an optically detected magnetic resonance (ODMR) spectrum in each pixel. From the resulting 2D map of NV resonance frequencies, we extract magnetic field components and crystal stress tensor elements (which have units of pressure). As crystal stress and strain are related through the compliance tensor (with 1050–1210 GPa Young's modulus for diamond, depending on orientation [9]), we refer to the crystal defects that induce stress within the diamond (shifting the NV ground-state sublevels and causing birefringence) as strain defects. We first demonstrate the NV stress imaging technique with diamond sample A, which contains a nitrogen-rich layer (25 ppm, 13 μm thick) grown on an electronic-grade single-crystal substrate with ppb nitrogen density. This sample was

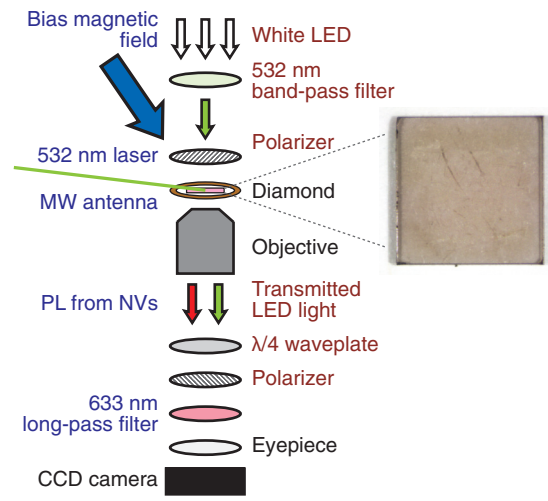

FIG. 1. Schematic of the combined NV stress and birefringence imager. The NV stress imager (blue labels) uses a 532-nm laser to illuminate the diamond, an applied microwave field to drive transitions between NV ground-state sublevels, and a bias magnetic field. The birefringence imager (maroon labels) uses a light-emitting diode (LED) illuminator, two linear polarizers, and a quarter-wave plate. Both imagers use the same microscope and CCD camera (black labels) to collect and image the transmitted light. The photograph on the right shows the diamond sample A studied in this work.

[*]Present address: Sandia National Laboratories, Albuquerque, NM 87123, USA.

electron irradiated and annealed to increase the NV density. We also apply the NV stress imaging technique to several other diamonds (samples B through J) [10,11], which also exhibit a variety of strain defects (see the Supplemental Material [12]).

Previous diamond strain imaging studies used x-ray topography, Raman spectroscopy, cathodoluminescence, and birefringence to characterize diamond strain and how it affects diamond applications [13–15]. By comparison, NV stress imaging gives a more direct characterization of how diamond stress inhomogeneity affects NV magnetic imaging, as both techniques probe the NV ODMR frequencies. In addition, NV stress imaging yields quantitative maps of the diamond stress tensor components localized in the NV layer with micrometer resolution [16]. The stress tensor reconstruction can help identify how strain features formed during diamond sample preparation and thereby inform future sample fabrication. Finally, high-resolution NV stress imaging is essential in ongoing efforts to identify damage tracks from recoiling carbon nuclei to search for high-energy particle collisions in diamond [17].

In the following sections, we describe NV stress imaging and compare NV-based and birefringence images acquired with the same optical microscope. We next consider how stress inhomogeneity compromises NV magnetometer sensitivity, and then present a survey of common strain defects found in fabricated diamond and their impacts on magnetic microscopy.

I. WIDEFIELD NV STRESS IMAGING

The NV center in diamond consists of a substitutional nitrogen atom in the carbon lattice adjacent to a vacancy [Fig. 2(a)]. It has an electronic spin-triplet ground state

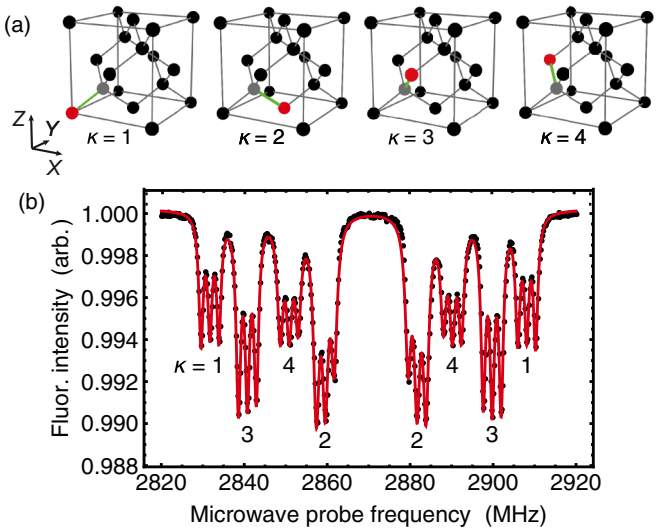

FIG. 2. (a) NV centers in the diamond lattice, with the four N-V axes shown in green [18]. Carbon atoms are black, nitrogen atoms are red, and vacancies are gray. (b) Example ODMR spectrum with $\vec{B} = \{220, 593, 1520\}$ μT in the diamond chip coordinate system (fit function plotted in red). The labels indicate the resonances from the different NV orientations. Each NV resonance is split into three lines due to hyperfine interactions with the spin-1 ^{14}N nucleus.

($S = 1$) with magnetic sublevels $m_s = \{-1, 0, +1\}$. The sublevel energies shift in response to local magnetic fields, crystal stress, temperature changes, and electric fields. We measure these energy (i.e., frequency) shifts using ODMR spectroscopy, where a resonant microwave field induces transitions between the $m_s = 0$ and ± 1 sublevels and causes reduced NV fluorescence under continuous illumination by 532-nm laser light [Fig. 2(b)]. Each NV is oriented along one of four crystallographic directions (labeled with the index $\kappa = \{1, 2, 3, 4\}$). An NV ensemble usually contains an equal number of NVs for each κ. The ODMR spectra from all NV orientations yields the information to reconstruct stress tensor elements and vector magnetic field components [3].

We now describe how to extract the local magnetic field and crystal stress from the measured NV resonance frequencies. The NV ground-state Hamiltonian in the presence of stress and a static magnetic field is [18–20]

$$\begin{aligned} H_\kappa =& (D + M_{z,\kappa})S_{z,\kappa}^2 + \gamma \vec{B} \cdot \vec{S}_\kappa \\ &+ M_{x,\kappa}\left(S_{y,\kappa}^2 - S_{x,\kappa}^2\right) \\ &+ M_{y,\kappa}(S_{x,\kappa}S_{y,\kappa} + S_{y,\kappa}S_{x,\kappa}) \\ &+ N_{x,\kappa}(S_{x,\kappa}S_{z,\kappa} + S_{z,\kappa}S_{x,\kappa}) \\ &+ N_{y,\kappa}(S_{y,\kappa}S_{z,\kappa} + S_{z,\kappa}S_{y,\kappa}). \end{aligned} \tag{1}$$

Here, $D \approx 2870$ MHz is the zero-field splitting, $S_{i,\kappa}$ are the dimensionless spin-1 projection operators, $\gamma = 2.803 \times 10^4$ MHz/T is the NV electronic gyromagnetic ratio, $\vec{B}$ is the magnetic field in the NV coordinate system, and $M_{i,\kappa}$ and $N_{i,\kappa}$ are terms related to the crystal stress and temperature. The indices $i = \{x, y, z\}$ represent the coordinate system for the particular NV orientation. We neglect the electric-field contributions to Eq. (1), as explained in the Supplemental Material [12,21]. In addition, if $|\vec{B}| > 1$ mT, as is the case in this work, the contributions from the $\{M_{x,\kappa}, M_{y,\kappa}, N_{x,\kappa}, N_{y,\kappa}\}$ terms are negligible, and Eq. (1) simplifies to

$$H_\kappa = (D + M_{z,\kappa})S_{z,\kappa}^2 + \gamma \vec{B} \cdot \vec{S}_\kappa. \tag{2}$$

When $\vec{B}$ is aligned along the z axis for one NV orientation, the Hamiltonian for the selected orientation reduces to

$$H_\kappa = (D + M_{z,\kappa})S_{z,\kappa}^2 + \gamma B_z S_{z,\kappa}, \tag{3}$$

and the resonance frequencies are

$$f_\pm = (D + M_{z,\kappa}) \pm \gamma B_z. \tag{4}$$

Measuring $f_\pm$ yields the magnetic field projection B_z and the $M_{z,\kappa}$ for that NV orientation. This measurement forms the basis of a sensing modality called projection magnetic microscopy (PMM) [3], where we align the bias magnetic field along the z axis of each NV orientation and record the associated resonance frequencies individually. An alternative sensing modality, called vector magnetic microscopy (VMM) [3], allows us to determine $\vec{B}$ and all four $M_{z,\kappa}$ terms from a single measurement [Fig. 2(b)]. In VMM, the selected bias magnetic field generates unique Zeeman splittings and nonoverlapping ODMR spectra for each NV orientation. We extract the magnetic field components and $M_{z,\kappa}$ values by fitting Eq. (2) for all four NV orientations. Both VMM and PMM yield the same $M_{z,\kappa}$ results; we detail advantages of

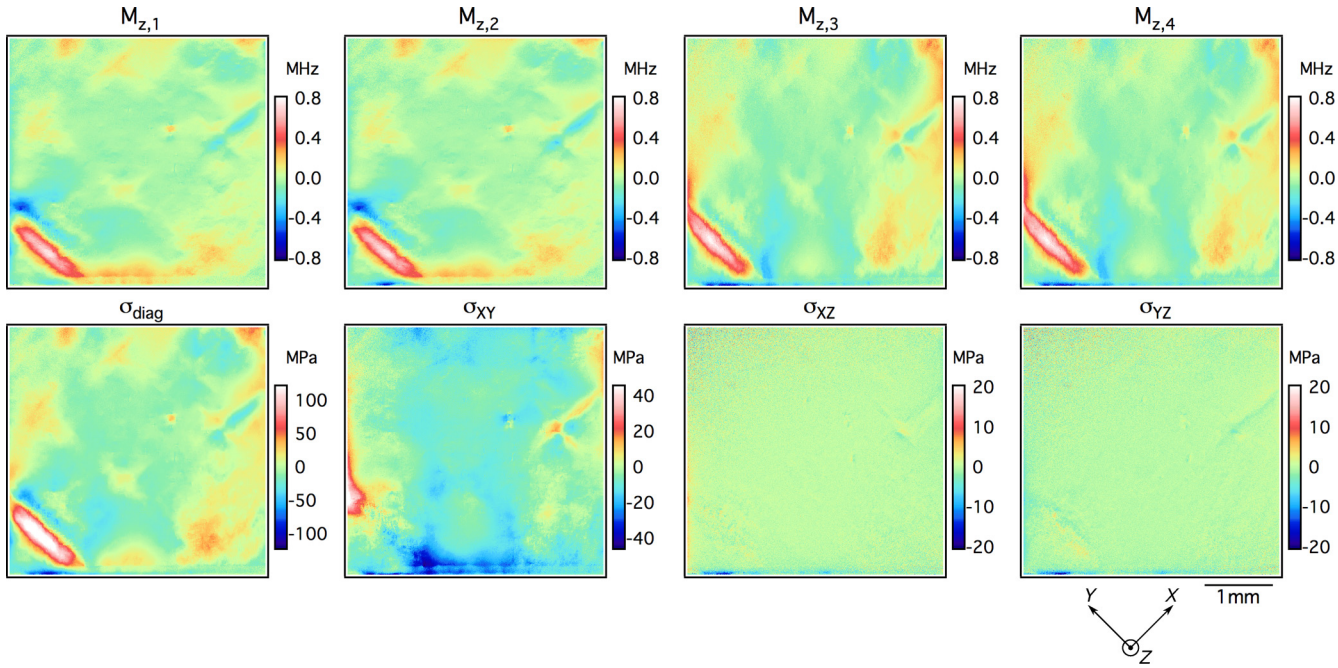

FIG. 3. Example NV $M_{z,\kappa}$ and $\{\sigma_{\text{diag}}, \sigma_{XY}, \sigma_{XZ}, \sigma_{YZ}\}$ maps for sample A. After measuring the $M_{z,\kappa}$ maps in the top row from the NV resonance frequencies, we calculate the stress tensor element maps in the bottom row using Eqs. (9)–(12). The diamond chip has high-stress and low-stress regions, and most of the $M_{z,\kappa}$ inhomogeneity comes from σ_{diag} and σ_{XY} stress terms.

each method in the Supplemental Material [12,22,23]. We used VMM in this work to measure the four necessary $M_{z,\kappa}$ maps (which we refer to as "NV $M_{z,\kappa}$ imaging") needed to reconstruct stress tensor elements for each pixel, as described below.

A. Stress tensor reconstruction

In each pixel, the stress tensor components can be determined from the four $M_{z,\kappa}$ parameters, allowing us to generate a quantitative image of the local stress across the diamond. Following the derivations in Refs. [18–20], we obtain

$$M_{z,1} = a_1\sigma_{\text{diag}} + 2a_2[\sigma_{XY} + \sigma_{XZ} + \sigma_{YZ}], \tag{5}$$

$$M_{z,2} = a_1\sigma_{\text{diag}} + 2a_2[\sigma_{XY} - \sigma_{XZ} - \sigma_{YZ}], \tag{6}$$

$$M_{z,3} = a_1\sigma_{\text{diag}} + 2a_2[-\sigma_{XY} + \sigma_{XZ} - \sigma_{YZ}], \tag{7}$$

$$M_{z,4} = a_1\sigma_{\text{diag}} + 2a_2[-\sigma_{XY} - \sigma_{XZ} + \sigma_{YZ}]. \tag{8}$$

Here, $\{a_1, a_2\} = \{4.86, -3.7\}$ MHz/GPa are spin-stress coupling constants [19], σ_{ij} are elements of the 3×3 stress tensor in GPa in the coordinate system shown in Fig. 2(a), and $\sigma_{\text{diag}} \equiv \sigma_{XX} + \sigma_{YY} + \sigma_{ZZ}$. The σ_{ii} are normal stress terms, while σ_{XY}, σ_{XZ}, and σ_{YZ} are shear stress terms. The σ_{ij} are written in the diamond unit cell coordinate system $\{X, Y, Z\}$ (rather than the NV coordinate system $\{x, y, z\}$ for a given κ) and are felt by all four NV orientations. Each NV orientation exhibits the same $a_1\sigma_{\text{diag}}$ contribution to $M_{z,\kappa}$. The a_2 contributions change as we transform the stress tensor for each of the four NV orientations.

Solving Eqs. (5)–(8) to extract σ_{diag}, σ_{XY}, σ_{XZ}, and σ_{YZ} in each pixel yields

$$\sigma_{\text{diag}} = \frac{1}{4a_1}[M_{z,1} + M_{z,2} + M_{z,3} + M_{z,4}], \tag{9}$$

$$\sigma_{XY} = \frac{1}{8a_2}[M_{z,1} + M_{z,2} - M_{z,3} - M_{z,4}], \tag{10}$$

$$\sigma_{XZ} = \frac{1}{8a_2}[M_{z,1} - M_{z,2} + M_{z,3} - M_{z,4}], \tag{11}$$

$$\sigma_{YZ} = \frac{1}{8a_2}[M_{z,1} - M_{z,2} - M_{z,3} + M_{z,4}]. \tag{12}$$

For the σ_{ii} normal stress terms, the measurements presented here are only sensitive to the total normal stress σ_{diag} rather than the individual σ_{ii} contributions [19]. A more sophisticated algorithm could use VMM spectra measured at several magnetic fields and keep all of the terms in Eq. (1) to obtain each σ_{ii} separately.

Since the $D + M_{z,\kappa}$ terms change with temperature, $M_{z,\kappa}$ and σ_{diag} can only be evaluated up to an overall constant [24,25]. However, the shear stress terms should be unaffected by temperature changes, and thus shear stress images are absolute. For measurements acquired with 10 mK temperature stability, an NV $M_{z,\kappa}$ imager can determine $M_{z,\kappa}$ to about 1 kHz, or ≈0.1 MPa. As a further example, a 1 μT/$\sqrt{\text{Hz}}$ magnetic sensitivity per pixel (28 kHz/$\sqrt{\text{Hz}}$ frequency sensitivity) corresponds to approximately 10 MPa/$\sqrt{\text{Hz}}$ stress sensitivity.

Figure 3 shows the measured $M_{z,\kappa}$ maps and the resulting $\{\sigma_{\text{diag}}, \sigma_{XY}, \sigma_{XZ}, \sigma_{YZ}\}$ maps for sample A, illustrating a practical example of NV $M_{z,\kappa}$ and stress imaging. This diamond has a variety of strain features (their origins are described below), in addition to more homogeneous regions. For sample A and most of the other diamond samples we investigated in this

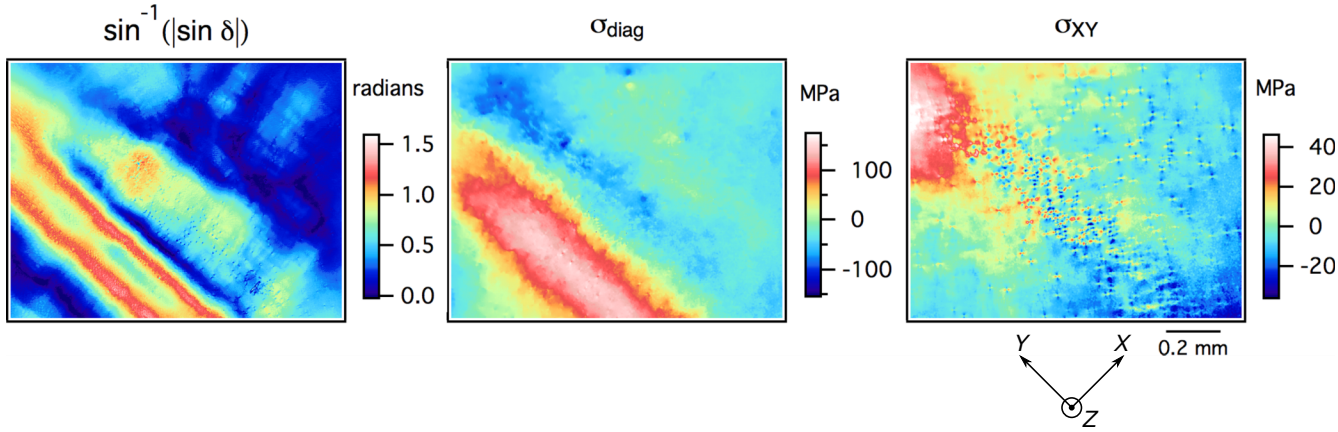

FIG. 4. Birefringence $\sin^{-1}|\sin\delta|$ and NV stress maps for the lower-left corner region of sample A. Both techniques show similar phenomena, though the NV stress imaging maps are immune to the $\delta > \pi/2$ phase ambiguity, can resolve the petal-shaped defects localized in the NV layer, separate out strain phenomena into different stress tensor contributions, and predict how strain features affect the NV magnetic microscopy performance.

work, we found the shear stress inhomogeneity was greater in σ_{XY} than in σ_{XZ} or σ_{YZ} [12]. The $M_{z,\kappa}$ variations were usually due to σ_{diag} and σ_{XY} inhomogeneity in roughly equal amounts.

II. COMPARISON WITH BIREFRINGENCE IMAGING

Here we compare NV stress imaging to birefringence imaging, which is a prominent characterization tool in the diamond community [13,26]. In this work, both methods were implemented within the same optical microscope for a straightforward comparison (Fig. 1). Both the NV $M_{z,\kappa}$ terms and the diamond refractive index depend on crystal stress, but NV stress imaging more directly captures relevant information about stress inhomogeneity in the NV layer and its effects on NV sensing. This makes NV stress imaging the more appropriate tool for optimizing NV diamond samples for magnetic microscopy.

In a birefringent material, light with orthogonal polarizations transmitted through a sample of thickness L accumulates a relative optical retardance phase $\delta = \frac{2\pi}{\lambda}\Delta n L$, where λ is the wavelength and Δn is the difference in refractive indices for orthogonal polarizations. We used a rotating-linear-polarizer method, also known as Metripol, to extract $|\sin\delta|$ by probing the sample with light of varying polarization angles [12,27–29]. The measured transmission intensity I_i for a given polarizer rotation angle α_i is

$$I_i = \tfrac{1}{2} I_0[1 + \sin 2(\alpha_i - \phi)\sin\delta]. \tag{13}$$

Here I_0 is the transmittance of a given pixel and ϕ is the retardance orientation angle. Sweeping α_i across 180° of polarization rotation allows us to determine I_0, $|\sin\delta|$, and ϕ [12].

Figure 4 shows a comparison between $\sin^{-1}|\sin\delta|$, σ_{diag}, and σ_{XY} maps collected using birefringence and NV stress imaging with the same diamond field of view. Despite the general similarity in results between the two methods, there are some stark differences. The σ_{XY} map shows petal-shaped strain features in the NV layer, whereas the birefringence map (which integrates phase retardance through the entire thickness) does not capture these fine details. Furthermore, the NV stress maps can distinguish that the diagonal stripe causing $M_{z,\kappa}$ inhomogeneity arises from σ_{diag} stress, while the petal-shaped strain features are caused by σ_{XY} stress. We can exploit such component-separated NV stress maps to investigate the sources and phenomenology of observed strain features.

Crystal strain and δ are linearly related through the diamond photoelastic parameters [30–33]. However, this relationship typically assumes uniform stress over the optical path, meaning that the δ we measure is integrated over L even though the strain may be localized to one layer. By comparison, the NV $M_{z,\kappa}$ technique provides stress information localized to the NV layer, and converting from $M_{z,\kappa}$ to stress tensor elements is more straightforward.

Figure 4 illustrates an additional limitation for birefringence imaging. For high-strain regions, the integrated δ through the sample thickness may be greater than $\pi/2$, leading to ambiguity when calculating stress from $|\sin\delta|$ since multiple δ values can yield the same $|\sin\delta|$. This occurs in the middle of the stripe feature in Fig. 4, where the reconstructed δ reaches its maximum value of $\pi/2$ before decreasing. NV stress imaging is not susceptible to this ambiguity. The NV σ_{diag} map instead shows that the stress amplitude increases to the middle of the stripe. Accounting for the extra $\approx\pi/4$ of phase accumulation in the birefringence map yields a maximum stress amplitude of ≈130 MPa, which is consistent with the 140 MPa maximum stress amplitude in the σ_{diag} map [12]. Despite the $|\sin\delta|$ ambiguity, the NV and birefringence methods yield consistent stress measurements.

III. STRESS AND NV MAGNETOMETRY

NV $M_{z,\kappa}$ inhomogeneity causes each NV in an ensemble to have different resonance frequencies, which reduces the magnetic sensitivity and degrades NV magnetometer performance [6]. A useful NV-magnetometer figure of merit is the slope of the ODMR line shape $|F'(f)|$, where f is the probe-microwave frequency and $F'(f)$ is the derivative of the NV fluorescence intensity at frequency f [Fig. 1(b)]. The maximum $|F'(f)|$ slope is proportional to the quantity C/Γ, where

C is the fluorescence contrast and Γ is the resonance linewidth [34]. $M_{z,\kappa}$ inhomogeneity reduces magnetic sensitivity by making the resonance line shape broader, the contrast weaker, and thus the maximum slope $|F'(f)| \propto C/\Gamma$ smaller [6].

For NV-diamond magnetometers that use fewer probe microwave frequencies for improved magnetic sensitivity, $M_{z,\kappa}$ inhomogeneity is even more detrimental. High-sensitivity magnetometers typically measure at two microwave frequencies (called the "two-point method") instead of probing the full width of the ODMR line shape (the "full-sweep method") [35]. The two microwave frequencies are typically chosen to maximize the two-point responsivity (defined as the change in fluorescence per unit frequency shift of the NV resonance). If $M_{z,\kappa}$ varies substantially over the field of view, no pair of frequencies can be optimal for all NVs, resulting in decreased sensitivity for many pixels in the magnetic image. A larger variation in $M_{z,\kappa}$ across the ensemble also implies a narrower magnetic-field range before the NVs in some pixels fall out of resonance. As such, $M_{z,\kappa}$ inhomogeneity limits the field of view and dynamic range of high-sensitivity NV magnetic imagers.

Figure 5 shows an enlarged $M_{z,\kappa}$ map together with single-pixel ODMR spectra corresponding to regions of sample A with different local strain properties. For example, one pixel shows a region with a low $M_{z,\kappa}$ gradient and offset from the mean (i); a second pixel shows a region with a low $M_{z,\kappa}$ gradient and a high $M_{z,\kappa}$ offset (ii); and a third pixel shows a region with a high $M_{z,\kappa}$ gradient and a low $M_{z,\kappa}$ offset (iii). These local strain conditions are caused by an $\approx$0.3 MHz $M_{z,\kappa}$ offset in the diagonal stripe and high $M_{z,\kappa}$ variation in the $\approx$30 μm petal defects. Pixels (i) and (ii) have a comparable C/Γ slope and therefore a comparable NV magnetic sensitivity when using the full-sweep method. However, when using the two-point method optimized for pixel (i), pixel (ii) will have a poor responsivity due to its large $M_{z,\kappa}$ offset. By comparison, pixel (iii) will exhibit poor performance with both methods. As these example pixels demonstrate, $M_{z,\kappa}$ inhomogeneity reduces the magnitude and uniformity of the magnetic sensitivity across an image.

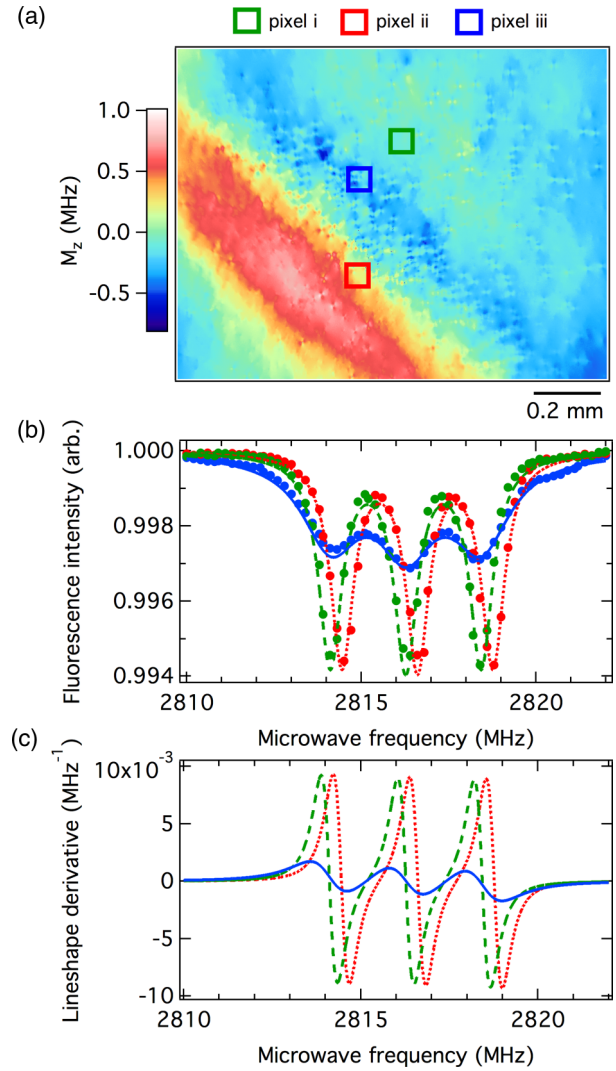

FIG. 5. (a) Enlarged $M_{z,\kappa}$ map (lower left corner of Fig. 3), showing the locations of the example pixels. (b) Fitted ODMR spectra for example pixels (i), (ii), and (iii) (green, red, and blue, respectively). Each has varying $M_{z,\kappa}$ gradients and offsets. (c) Derivatives $F'(f)$ for the ODMR line shapes plotted in panel (b). Pixel (i) has the best C/Γ slope and two-point responsivity, while pixel (ii) has a good C/Γ slope but a poor two-point responsivity since the $M_{z,\kappa}$ offset means we probe this pixel at a suboptimal microwave frequencies compared to the others. Pixel (iii) has poor C/Γ slope and two-point responsivity due to the high $M_{z,\kappa}$ inhomogeneity in this pixel.

IV. STRAIN FEATURE SURVEY AND EFFECTS ON NV MAGNETOMETRY

We used NV $M_{z,\kappa}$ imaging to study and categorize different types of strain features in diamond samples. As shown in the regions highlighted in Fig. 6, different types of strain features have a variety of typical dimensions, $M_{z,\kappa}$ amplitudes and gradients, and stress tensor contributions. From our $M_{z,\kappa}$ maps, we categorized strain features into general types. We identified how each type impacts the C/Γ slope and two-point responsivity. Here we concentrate on strain features observed in sample A. Surveys of additional diamonds exhibiting similar phenomena are included in the Supplemental Material [12].

Figure 6(a) shows the same field of view as in Fig. 5. The broad-scale plastic deformation in the diagonal stripe is perhaps associated with the lower-left corner of the diamond sample, as high stress is common at sharp corners, edges, and fractures. The stress from the diagonal stripe is largely σ_{diag} stress, causing millimeter-scale $M_{z,\kappa}$ gradients, resulting in a wide span in NV resonance frequencies ($\approx$1 MHz). As anticipated, the diagonal stripe spoils the two-point responsivity while the full-sweep C/Γ slope is largely unaffected. In this example, the $M_{z,\kappa}$ span is large enough to cause a negative responsivity in the diagonal stripe, as the resonance frequency is offset far enough that one of the probe frequencies is on the opposite side of its resonance peak.

The 20- to 30-μm petal-shaped strain defects in Fig. 6(a) and Fig. 4 are caused by lattice dislocations that can form on top of the seed crystal during homoepitaxial growth, as studied in previous work [13,26,36–38]. The three types of lattice dislocations (edge, screw, and mixed dislocations) contribute to different crystal stress terms [39]. The petal features appear

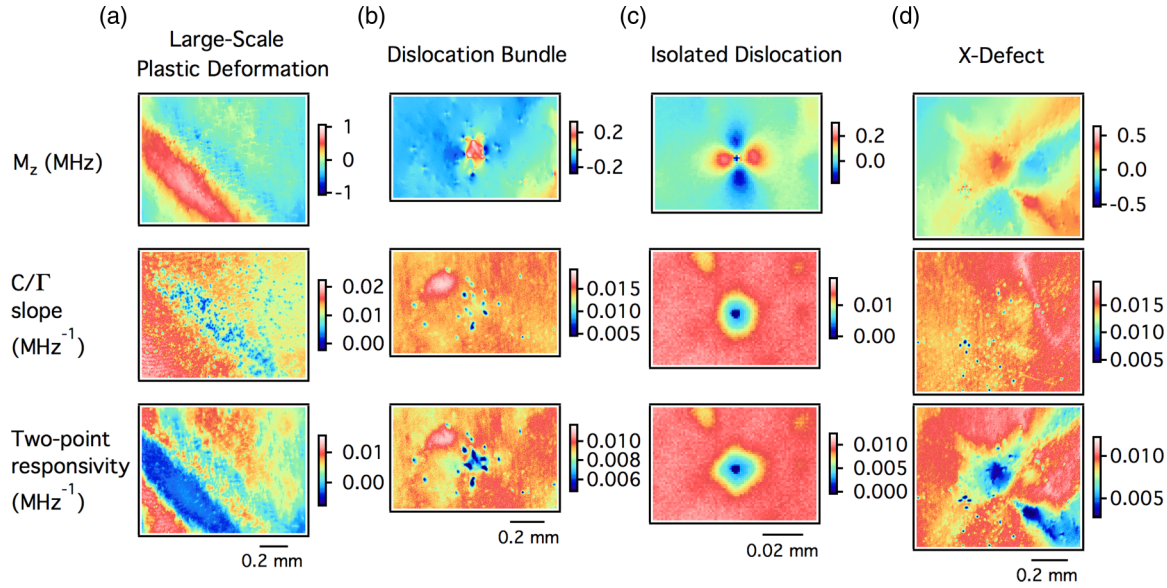

FIG. 6. Comparisons between $M_{z,\kappa}$, C/Γ slope, and two-point responsivity for common strain feature types found in sample A. The C/Γ and responsivity maps are related to the magnetic microscopy performance when using the full-sweep method and the two-point method, respectively. Note that the two-point responsivity is more susceptible to $M_{z,\kappa}$ inhomogeneity, while the full-sweep method can tolerate some range of $M_{z,\kappa}$ offsets.

most strongly in the σ_{diag} and σ_{XY} maps (and to a lesser degree in the σ_{XZ} and σ_{YZ} maps), which suggests that the petal-shaped strain features we observed are predominantly caused by edge and mixed dislocations.

Figure 6(b) shows a ≈200-μm strain feature (likely caused by a dislocation bundle), surrounded by smaller petal-shaped defects. From birefringence imaging, we know that such strain features are typically edge dislocations (with σ_{diag} and σ_{XY} stress). They often have four quadrants with lines emanating from the center along the [001] and [010] directions, and are a few hundred micrometers across [40,41]. As shown in the Supplemental Material [12], the birefringence map displays lobes associated with the strain feature in Fig. 6(b), with the expected orientation. The lobes appearing in the σ_{diag} and σ_{XY} NV stress maps are rotated by 45°. These characteristics lead us to conclude that this strain feature is a dislocation bundle. For this particular strain feature, the range of $M_{z,\kappa}$ values is narrow enough that it has only a minor effect on NV magnetometry performance for both the full-sweep and two-point methods.

Figure 6(c) shows a prominent ≈30-μm dislocation strain feature. Here the single-pixel $M_{z,\kappa}$ gradients are substantial enough to spoil the NV magnetic sensitivity of both methods. Severe $M_{z,\kappa}$ gradients also interfere when fitting the ODMR spectra to a Lorentzian line-shape model, introducing systematic errors in the extracted resonance frequencies. Such errors can produce false features in NV magnetic images [12].

Figure 6(d) shows a ≈0.8-mm X-shaped strain feature. Though visually most similar to the petal-shaped strain features discussed above, X-shaped strain features are larger, display sharp edges pointing along the diamond [100] and [010] directions, and have no lobe structures. The X-shaped strain features also exhibit mainly σ_{diag} and σ_{XY} stress (like an edge dislocation), whereas the σ_{XZ} and σ_{YZ} values are nearly zero. Despite the similarities to the previously discussed strain features, the origin of the X-shaped strain features remains under investigation. They mainly affect the two-point responsivity for NV magnetometry, whereas the full-sweep C/Γ slope is mostly immune.

V. SUMMARY AND OUTLOOK

We presented a method for quantitative stress imaging in diamond with micrometer spatial resolution and millimeter field of view using a layer of NV centers. We compared NV stress imaging to the more traditional birefringence imaging method, implemented in the same experimental setup, and found quantitative and qualitative consistency. NV $M_{z,\kappa}$ imaging offers a straightforward way to reconstruct stress tensor elements within a diamond sample and provides a more direct measure of how the strain features affect NV magnetic imaging. NV $M_{z,\kappa}$ imaging is therefore a useful tool to support NV magnetic microscopy and other diamond applications that rely on crystal homogeneity for optimal performance.

To further improve the NV $M_{z,\kappa}$ imaging method, one can implement NV sensitivity and resolution enhancements. For example, one can boost the sensitivity by implementing a double-quantum Ramsey spectroscopy protocol, creating a superposition of the NV $m_s = \pm 1$ magnetic sublevels. This doubles the $M_{z,\kappa}$ part of Eq. (2) and cancels the magnetic contribution [6,42]. NV $M_{z,\kappa}$ imaging with double-quantum Ramsey spectroscopy should be beneficial for NV layers where the magnetic field inhomogeneity dominates the $M_{z,\kappa}$ inhomogeneity. Furthermore, for specific applications, one can perform additional measurements to disentangle the σ_{ii} normal stress terms. Finally, one can employ NV super-resolution techniques to map the stress tensor components with a resolution beyond the optical diffraction limit [43,44].

Looking to future diamond applications for particle physics, diamond stress characterization is important for the recently proposed diamond directional weakly interacting massive particle (WIMP) detector [17]. This approach aims to use NV centers to image the stress created by ≈100-nm tracks from recoiling carbon nuclei. Mapping the intrinsic $M_{z,\kappa}$ and stress inhomogeneity is a first step to exploring the feasibility of directional WIMP detection with NVs. In particular, since σ_{XZ} and σ_{YZ} stresses are typically smaller than σ_{diag} and σ_{XY} stresses, detecting deviations in σ_{XZ} or σ_{YZ} may exhibit a larger signal-to-background ratio. Anticipated next steps include NV $M_{z,\kappa}$ imaging with higher spatial resolution (<1 μm) and variable depth, cataloging the $M_{z,\kappa}$ distribution from many individual NV centers in a low-density bulk sample (ppb NV density), investigating hybrid-sensor schemes (such as a combined cathodoluminescence/$M_{z,\kappa}$ method) to rapidly survey diamond chips for damaged voxels, and imaging the recoil tracks from implanted ^{12}C nuclei.

Recently, we became aware of a preprint [16] which presents a similar NV stress mapping scheme, though our work studies naturally-formed defects to optimize NV magnetic imaging.

ACKNOWLEDGMENTS

We thank Marcus Doherty and Adam Gali for help with clarifying the crystal stress contributions to the NV Hamiltonian and Michel Mermoux for insights on stress tensor extraction methods. We thank Patrick Scheidegger for assistance adopting GPU-accelerated data analysis and Connor Finnerty for assistance in automating the birefringence imaging. We also thank Abdelghani Laraoui, Andrew Mounce, and David Phillips for providing feedback on the manuscript. J.M.S. was supported by a Fannie and John Hertz Foundation Graduate Fellowship and a National Science Foundation Graduate Research Fellowship under Grant No. 1122374. This work was supported by DOE Award No. DE-SC0019396; DARPA DRINQS Award No. D18AC00033; Air Force Office of Scientific Research Award No. FA9550-17-1-0371; and NSF Awards No. PHY-1504610 and No. EAR 1647504. This work was performed in part at the Harvard Center for Nanoscale Systems (CNS), a member of the National Nanotechnology Coordinated Infrastructure Network (NNCI), which is supported by the National Science Foundation under NSF Award No. 1541959. We thank Edward Soucy, Brett Graham, and the Harvard Center for Brain Science for technical support and fabrication assistance.

[1] Y. Schlussel, T. Lenz, D. Rohner, Y. Bar-Haim, L. Bougas, D. Groswasser, M. Kieschnick, E. Rozenberg, L. Thiel, A. Waxman, J. Meijer, P. Maletinsky, D. Budker, and R. Folman, Phys. Rev. Appl. **10**, 034032 (2018).

[2] J.-P. Tetienne, N. Dontschuk, D. A. Broadway, A. Stacey, D. A. Simpson, and L. C. L. Hollenberg, Sci. Adv. **3**, e1602429 (2017).

[3] D. R. Glenn, R. R. Fu, P. Kehayias, D. Le Sage, E. A. Lima, B. P. Weiss, and R. L. Walsworth, Geochem., Geophys., Geosyst. **18**, 3254 (2017).

[4] D. Le Sage, K. Arai, D. R. Glenn, S. J. DeVience, L. M. Pham, L. Rahn-Lee, M. D. Lukin, A. Yacoby, A. Komeili, and R. L. Walsworth, Nature (London) **496**, 486 (2013).

[5] I. Fescenko, A. Laraoui, J. Smits, N. Mosavian, P. Kehayias, J. Seto, L. Bougas, A. Jarmola, and V. M. Acosta, Phys. Rev. Appl. **11**, 034029 (2019).

[6] E. Bauch, C. A. Hart, J. M. Schloss, M. J. Turner, J. F. Barry, P. Kehayias, S. Singh, and R. L. Walsworth, Phys. Rev. X **8**, 031025 (2018).

[7] J. F. Barry, M. J. Turner, J. M. Schloss, D. R. Glenn, Y. Song, M. D. Lukin, H. Park, and R. L. Walsworth, Proc. Natl. Acad. Sci. USA **113**, 14133 (2016).

[8] K. Jensen, N. Leefer, A. Jarmola, Y. Dumeige, V. M. Acosta, P. Kehayias, B. Patton, and D. Budker, Phys. Rev. Lett. **112**, 160802 (2014).

[9] K. E. Spear and J. P. Dismukes, *Synthetic Diamond: Emerging CVD Science and Technology* (Wiley, New York, 1994).

[10] M. P. Backlund, P. Kehayias, and R. L. Walsworth, Phys. Rev. Appl. **8**, 054003 (2017).

[11] H. C. Davis, P. Ramesh, A. Bhatnagar, A. Lee-Gosselin, J. F. Barry, D. R. Glenn, R. L. Walsworth, and M. G. Shapiro, Nat. Commun. **9**, 131 (2018).

[12] See Supplemental Material at http://link.aps.org/supplemental/10.1103/PhysRevB.100.174103 for additional details.

[13] I. Friel, S. Clewes, H. Dhillon, N. Perkins, D. Twitchen, and G. Scarsbrook, Diam. Relat. Mater. **18**, 808 (2009).

[14] A. Crisci, F. Baillet, M. Mermoux, G. Bogdan, M. Nesládek, and K. Haenen, Phys. Status Solidi (A) **208**, 2038 (2011).

[15] P. L. Hanley, I. Kiflawi, and A. R. Lang, Proc. Philos. Trans. Royal Soc. **284**, 329 (1977).

[16] D. A. Broadway, B. C. Johnson, M. S. J. Barson, S. E. Lillie, N. Dontschuk, D. J. McCloskey, A. Tsai, T. Teraji, D. A. Simpson, A. Stacey, J. C. McCallum, J. E. Bradby, M. W. Doherty, L. C. L. Hollenberg, and J.-P. Tetienne, Nano Lett. **19**, 4543 (2019).

[17] S. Rajendran, N. Zobrist, A. O. Sushkov, R. Walsworth, and M. Lukin, Phys. Rev. D **96**, 035009 (2017).

[18] A. Barfuss, M. Kasperczyk, J. Kölbl, and P. Maletinsky, Phys. Rev. B **99**, 174102 (2019).

[19] M. S. J. Barson, P. Peddibhotla, P. Ovartchaiyapong, K. Ganesan, R. L. Taylor, M. Gebert, Z. Mielens, B. Koslowski, D. A. Simpson, L. P. McGuinness, J. McCallum, S. Prawer, S. Onoda, T. Ohshima, A. C. Bleszynski Jayich, F. Jelezko, N. B. Manson, and M. W. Doherty, Nano Lett. **17**, 1496 (2017).

[20] P. Udvarhelyi, V. O. Shkolnikov, A. Gali, G. Burkard, and A. Pályi, Phys. Rev. B **98**, 075201 (2018).

[21] M. W. Doherty, F. Dolde, H. Fedder, F. Jelezko, J. Wrachtrup, N. B. Manson, and L. C. L. Hollenberg, Phys. Rev. B **85**, 205203 (2012).

[22] K. Ohno, F. J. Heremans, L. C. Bassett, B. A. Myers, D. M. Toyli, A. C. B. Jayich, C. J. Palmstrom, and D. D. Awschalom, Appl. Phys. Lett. **101**, 082413 (2012).

[23] M. W. Doherty, V. V. Struzhkin, D. A. Simpson, L. P. McGuinness, Y. Meng, A. Stacey, T. J. Karle, R. J. Hemley,

N. B. Manson, L. C. L. Hollenberg, and S. Prawer, Phys. Rev. Lett. **112**, 047601 (2014).

[24] V. M. Acosta, E. Bauch, M. P. Ledbetter, A. Waxman, L.-S. Bouchard, and D. Budker, Phys. Rev. Lett. **104**, 070801 (2010).

[25] M. W. Doherty, V. M. Acosta, A. Jarmola, M. S. J. Barson, N. B. Manson, D. Budker, and L. C. L. Hollenberg, Phys. Rev. B **90**, 041201(R) (2014).

[26] L. T. M. Hoa, T. Ouisse, D. Chaussende, M. Naamoun, A. Tallaire, and J. Achard, Cryst. Growth Des. **14**, 5761 (2014).

[27] A. M. Glazer, J. G. Lewis, and W. Kaminsky, Proc. R. Soc. London A **452**, 2751 (1996).

[28] M. A. Geday, W. Kaminsky, J. G. Lewis, and A. M. Glazer, J. Microsc. **198**, 1 (2000).

[29] W. Kaminsky, E. Gunn, R. Sours, and B. Kahr, J. Microsc. **228**, 153 (2007).

[30] D. Howell, Eur. J. Mineral. **24**, 575 (2012).

[31] J. F. Nye, *Physical Properties of Crystals* (Oxford University Press, Oxford, UK, 1957).

[32] G. N. Ramachandran, Proc. Indian Acad. Sci., Sect. A **26**, 77 (1947).

[33] L. S. Hounsome, R. Jones, M. J. Shaw, and P. R. Briddon, Phys. Status Solidi (A) **203**, 3088 (2006).

[34] K. Jensen, P. Kehayias, and D. Budker, Magnetometry with nitrogen-vacancy centers in diamond, in *High Sensitivity Magnetometers*, edited by A. Grosz, M. J. Haji-Sheikh, and S. C. Mukhopadhyay (Springer International, Cham, 2017), pp. 553–576.

[35] D. R. Glenn, D. B. Bucher, J. Lee, M. D. Lukin, H. Park, and R. L. Walsworth, Nature (London) **555**, 351 (2018).

[36] M. Gaukroger, P. Martineau, M. Crowder, I. Friel, S. Williams, and D. Twitchen, Diam. Relat. Mater. **17**, 262 (2008).

[37] N. Tsubouchi, Y. Mokuno, H. Yamaguchi, N. Tatsumi, A. Chayahara, and S. Shikata, Diam. Relat. Mater. **18**, 216 (2009).

[38] P. M. Martineau, S. C. Lawson, A. J. Taylor, S. J. Quinn, D. J. F. Evans, and M. J. Crowder, Gems Gemol. **40**, 2 (2004).

[39] D. Hull and D. Bacon, *Introduction to Dislocations*, 5th ed. (Butterworth-Heinemann, Oxford, UK, 2011).

[40] H. Pinto and R. Jones, J. Phys.: Condens. Matter **21**, 364220 (2009).

[41] H. Pinto, R. Jones, J. P. Goss, and P. R. Briddon, J. Phys.: Conf. Ser. **281**, 012023 (2011).

[42] D. M. Toyli, C. F. de las Casas, D. J. Christle, V. V. Dobrovitski, and D. D. Awschalom, Proc. Natl. Acad. Sci. USA **110**, 8417 (2013).

[43] E. Rittweger, K. Y. Han, S. E. Irvine, C. Eggeling, and S. W. Hell, Nat. Photon. **3**, 144 (2009).

[44] J.-C. Jaskula, E. Bauch, S. Arroyo-Camejo, M. D. Lukin, S. W. Hell, A. S. Trifonov, and R. L. Walsworth, Opt. Express **25**, 11048 (2017).